

# Iron-based superconductivity extended to the novel hydride LaFeSiH

F. Bernardini,<sup>1</sup> G. Garbarino,<sup>2</sup> A. Sulpice,<sup>3</sup> M. Núñez-Regueiro,<sup>3</sup>  
E. Gaudin,<sup>4</sup> B. Chevalier,<sup>4</sup> A. Cano,<sup>4,\*</sup> and S. Tencé<sup>4</sup>

<sup>1</sup>*CNR-IOM-Cagliari and Dipartimento di Fisica,  
Università di Cagliari, IT-09042 Monserrato, Italy*

<sup>2</sup>*European Synchrotron Radiation Facility, 6 rue Jules Horowitz, BP 220, 38043 Grenoble, France*

<sup>3</sup>*CNRS, Université Grenoble Alpes, Institut Néel, 38042 Grenoble, France*

<sup>4</sup>*CNRS, Univ. Bordeaux, ICMCB, UPR 9048, F-33600 Pessac, France*

(Dated: June 6, 2022)

We report the synthesis and characterization of the novel hydride LaFeSiH displaying superconductivity below 9 K. We find that this pnictogen-free compound is isostructural to LaFeAsO, with a similar low-temperature tetragonal to orthorhombic distortion. Using density functional theory we show that this system is also a multiband metal in which the orthorhombic distortion is likely related to single-stripe antiferromagnetic order. Electrical resistivity and magnetic susceptibility measurements reveal that these features occur side-by-side with superconductivity, which is suppressed by external pressure.

Iron-based superconductors (Fe-based SCs) provide an unprecedented playground for the investigation of high- $T_c$  superconductivity. These systems belong to a huge family of compounds and recurrently display the following key features (see e.g. [1] for recent reviews). From the structural point of view, they have FeX layers in which the Fe atoms form a square lattice that is sandwiched between two ( $\sqrt{2} \times \sqrt{2}$ ) $R45^\circ$  shifted lattices of X (= P, As, Se, Te, S). This leads to a quasi-2D multiband Fermi surface that mainly originates from the Fe 3d orbitals. In addition, the parent compounds often display anti-ferromagnetic (AFM) order which is closely followed by a structural transformation (the so-called nematic transition). In the prototypical case of RFeAsO (R = rare earth), for example, this specifically corresponds to single-stripe AFM order [also called ( $\pi, 0$ ) order] and a square-to-rectangular distortion of the Fe layers. These features advocate for the so-called  $s_\pm$  superconducting gap symmetry and a spin-fluctuation pairing. This superconductivity can be induced by carrier doping resulting from either chemical substitutions or physical pressure [2]. From a more methodological point of view, the electronic band structure and the magnetic orders found in Fe-based SC can be reasonably well described by means of DFT-based calculations as the electronic correlations often remain relatively weak.

The search for novel Fe-based SC has been naturally extended to systems in which the FeX layer contains group IV elements such as Si and Ge. Thus, MgFeGe for example has been identified as isostructural and isoelectronic to the LiFeAs compound but displaying no superconductivity [3–5]. Evidence for superconductivity below 2 K has recently been reported in YFe<sub>2</sub>Ge<sub>2</sub> [6, 7], although whether bulk superconductivity is actually realized in this material is currently under debate [8]. On the other hand, hydrogen substitution has proven to be a particularly interesting route to induce superconductivity in these systems. Specifically, the carrier doping limit

of the original F substitution in LaFeAsO has been surpassed with hydrogen, thus revealing a two-dome superconductivity [9] together with a second magnetic phase in the additional parent compound LaFeAsO<sub>0.5</sub>H<sub>0.5</sub> [10]. In this paper, we report the synthesis, crystal structure and physical properties of the novel compound LaFeSiH. In addition, we study the behavior of the system under hydrostatic pressure and perform density-functional-theory (DFT) calculations to obtain the corresponding electronic band structure and magnetic ground state of this compound. Thus, we find that the new compound LaFeSiH is isostructural, isoelectronic and also “isomagnetic” to the 1111 family of Fe-based SC. Most importantly, we find superconductivity below 9 K in this pnictide- and chalcogenide-free system.

*Crystal structure.*— We synthesized the hydride LaFeSiH as described in the Supplemental Material, and obtained two powder samples (sam1 and sam2 in the following). The compound is stable in air, and its room-temperature crystal structure corresponds to the tetragonal space group  $P4/nmm$  with the structural parameters shown in Table I. This structure was determined from the Rietveld refinement of the x-ray powder diffraction pattern and more accurately from single-crystal x-ray diffraction measurements (see Fig. 1 and Supplemental Material). Compared to LaFeSi [11], the new compound displays a variation of the lattice parameters that is highly anisotropic:  $a = 4.098 \rightarrow 4.027$  Å and  $c = 7.133 \rightarrow 8.014$  Å. This variation is due to the hydrogen insertion at the  $2b$  Wyckoff position, as observed in other CeFeSi-type hydrogenated intermetallics [12]. This insertion is confirmed from the single-crystal x-ray diffraction pattern. Additionally, we performed DFT calculations in which we confirmed that the  $2b$  position is a very stable position for the H atom. Specifically, the overall  $P4/nmm$  structure is found to have a well-defined phonon spectrum with H-related optical phonons of frequencies greater than 100.5 meV. Thus, we conclude that

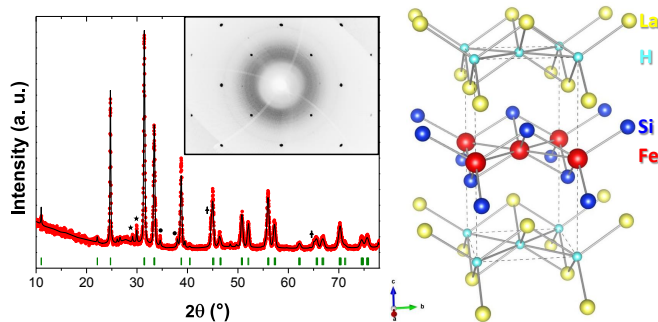


FIG. 1. (Left) Room temperature X-ray powder diffraction pattern of LaFeSiH (sam1). Ticks indicate the Bragg peaks of the  $P4/nmm$  structure of the main LaFeSiH phase while stars, crosses and circles indicate extra peaks due to the secondary phases  $\text{La}_2\text{O}_3$ ,  $\alpha\text{-Fe}$  and  $\text{La}(\text{Fe},\text{Si})_{13}\text{H}_x$  respectively that could not be completely eliminated by annealing. The  $(hk0)$ -plane of the LaFeSiH single-crystal diffraction pattern at room temperature is shown in the inset. (Right) Ball-and-stick model of the crystal structure of LaFeSiH.

the room-temperature crystal structure of LaFeSiH is essentially the same structure of the 1111 Fe-based SCs (e.g. LaFeAsO) as illustrated in Fig. 1.

We also determined the low-temperature crystal structure by performing additional x-ray synchrotron experiments at 15 K. The refinement of the corresponding structure revealed a low-temperature phase of LaFeSiH with space group symmetry  $Cmma$ . The structural parameters of this phase are in Table I. The orthorhombic distortion is rather small, which is again similar to the observed in Fe-based SCs.

*Electronic and magnetic structure.*— We first computed the electronic structure of LaFeSiH assuming a non-magnetic ground state (see Supplemental Material for details). We took the experimental low-temperature structural parameters as input. However, since the orthorhombic distortion is very small, we averaged the  $a$  and  $b$  parameters and considered an effective tetragonal structure. In Fig. 2 (top-right) we show the calculated electronic density of states (DOS) and the partial DOS (PDOS) projected on the Fe  $3d$  orbitals. As we can see, the system has a metallic nature with a DOS at the Fermi level that is largely dominated by the Fe- $3d$  orbitals. The corresponding band structure is shown in Fig. 2 (top-left), where the size of the symbols reflects the PDOS of the  $3(d_{xz} + d_{yz})$  Fe orbitals. This structure reveals the presence of several bands crossing the Fermi energy, which renders the system a multiband character. Specifically, we have two hole bands centered at the  $\Gamma$  point and two additional bands around the  $M$  point. In addition, there is a third band centered at the  $\Gamma$  point below the Fermi energy but very close. The resulting Fermi surface is shown in Fig. 2 (bottom). This Fermi surface has a resemblance to the characteristic Fermi surface of the Fe-based SCs. The central lobe originating from the

293K - $P4/nmm$ (#129, origin 2)				
$a = 4.0270(1)\text{\AA}$ $c = 8.0374(8)\text{\AA}$				
Wyckoff pos.	$x$	$y$	$z$	
La	2c	1/4 1/4	0.6722(1)	
Fe	2a	3/4 1/4	0	
Si	2c	1/4 1/4	0.1500(5)	
H	2b	3/4 1/4	1/2	

15K - $Cmma$ (#67)				
$a = 5.6831(6)\text{\AA}$ $b = 5.7039(6)\text{\AA}$ $c = 7.9728(6)\text{\AA}$				
Wyckoff pos.	$x$	$y$	$z$	
La	4g	0 1/4	0.1747(3)	
Fe	4b	1/4 0	0	
Si	4g	0 1/4	0.655(1)	
H	4a	1/4 0	0	

TABLE I. Structure parameters of LaFeSiH. (293K) The atomic positions were obtained from single-crystal x-ray diffraction performed on a  $2.6 \times 1.5 \times 1.7 \mu\text{m}^3$  crystal singled out from sam1 and the cell parameters determined from the powder. The diffraction pattern of this high-quality single-crystal reveals the  $2b$  position of the H atom. Its refinement, however, is restricted to the La, Fe, and Si atoms. (15K) Parameters obtained from Rietveld refinements of x-ray synchrotron data.

outer hole band and the belly of the otherwise cylindrical electron sheets represent the main differences.

The nesting properties of the LaFeSiH Fermi surface are limited compared to most of Fe-based SCs. Yet this system can develop some type of magnetic order. Thus, we performed additional DFT calculations in which dif-

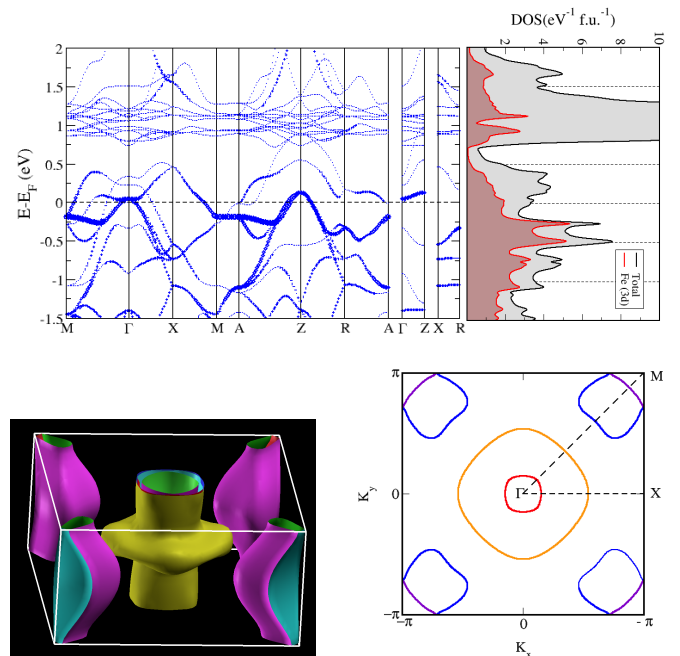


FIG. 2. (Top-left) Band structure and (top-right) total DOS and PDOS of the Fe- $3d$  states. (Bottom-left) Three dimensional view of the Fermi surface and (bottom-right) cross section in the  $k_z = 0$  plane.

ferent magnetic states were considered. Specifically, we study the tendency of the non-magnetic tetragonal structure towards ferromagnetic (FM), single-stripe AFM, double-stripe AFM and checkerboard AFM ordering of the Fe spins. The energy difference with respect to the non-magnetic state and the corresponding magnetic moments are reported in Table II. We find that the single-stripe AFM order reduces considerably the total energy of the system, and therefore is expected to be the ground state of the system. This explains the orthorhombic distortion we observed experimentally, as this is expected to be a by-product of the single-stripe AFM order triggered by magnetostructural coupling [13–15].

*Crystal and magnetic structure under pressure.*— Next, we study the orthorhombic low-temperature structure of the system under external pressure. In Fig. 3 we show the evolution of the orthorhombic distortion at 15 K obtained from our x-ray synchrotron measurements on sam1. We find that this distortion is suppressed by the application of external pressure and eventually disappears at  $P_{c1} \simeq 9.4$  GPa. This is similar to the observed in most of Fe-based SCs. Interestingly, by further increasing the pressure the structural distortion re-emerges at  $P_{c2} \simeq 12.7$  GPa. This behavior strongly resembles the observed in LaFeAsO by means of H doping [10].

In order to elucidate the nature of the high-pressure state we performed additional DFT calculations as a function of pressure for the aforementioned magnetic configurations. In these calculations, the single-stripe AFM state was always found to be the lowest-energy state. In Fig. 4 we show the resulting Fe magnetic moment and the energy difference with respect to the non-magnetic state as a function of pressure. Although the precise numerical values depend on the DFT method, they are in remarkably good agreement with the experimental observations. Namely, the application of external pressure first produces the suppression of single-stripe AFM order which then re-emerges as the pressure is further increased. Moreover, according to these results, the re-emergence is expected to be discontinuous. The rea-

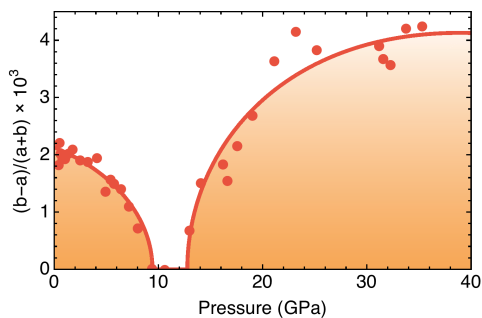


FIG. 3. Relative difference between the  $a$  and  $b$  lattice parameters of LaFeSiH at 15K as a function of pressure. Lines are guides to the eye.

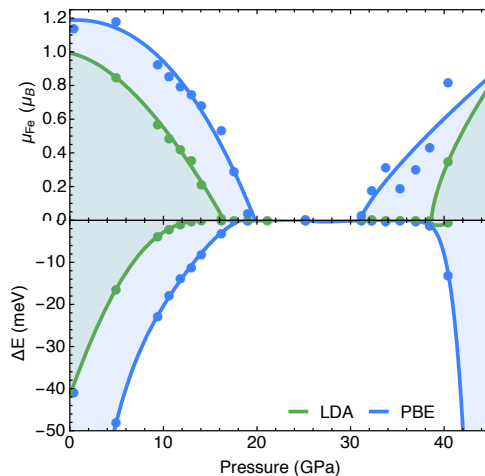


FIG. 4. Calculated Fe magnetic moment in the single-stripe AFM state (top) and energy difference with respect to the non-magnetic state (bottom) as a function of pressure. The results obtained with LDA and PBE functionals are represented by blue and green points respectively. Lines are guides to the eye.

son is that, even if a non-vanishing Fe magnetic moment is developed, the energy of the single-stripe AFM state requires some extra pressure to eventually become lower than the energy of the non-magnetic state. The structural distortion observed in our experiments, however, displays rather continuous behavior. Note that this distortion is just a by-product of the magnetic order induced by magnetostructural coupling, and hence is quite small. Consequently, the magnetic discontinuity expected from the DFT calculations could be very difficult to observe indirectly via the lattice distortion. In any case, these calculations are remarkably consistent with the structural behavior observed in our x-ray experiments (see Fig. 3).

*Magnetization and electrical resistivity.*— The magnetic response of our samples undoubtedly reveals the emergence of superconductivity in LaFeSiH. Due to the synthesis method, the presence of the secondary ferromagnetic phases  $\alpha$ -Fe and  $\text{La}(\text{Fe},\text{Si})_{13}\text{H}_x$  produces a zero-field initial magnetization at low temperatures. However, we find a negative initial slope of the overall magnetization as a function of magnetic field that can be as strong as  $dM/dH \sim -1.44 \times 10^{-2}$  emu/cm<sup>3</sup> [see Fig. 5 (a)]. This implies a global diamagnetic response whose strength is  $4.4 \times 10^2$  higher than that of pyrolytic car-

	checkerboard	FM	double-stripe	single-stripe
$\Delta E$ (meV/Fe)	-5.71	-11.11	-11.26	<b>-44.56</b>
$\mu_{\text{Fe}}$ ( $\mu_{\text{B}}$ )	0.90	0.65	1.04	1.16

TABLE II. Energy difference with respect to the non-magnetic state and Fe magnetic moments for various magnetic configurations obtained from DFT calculations.

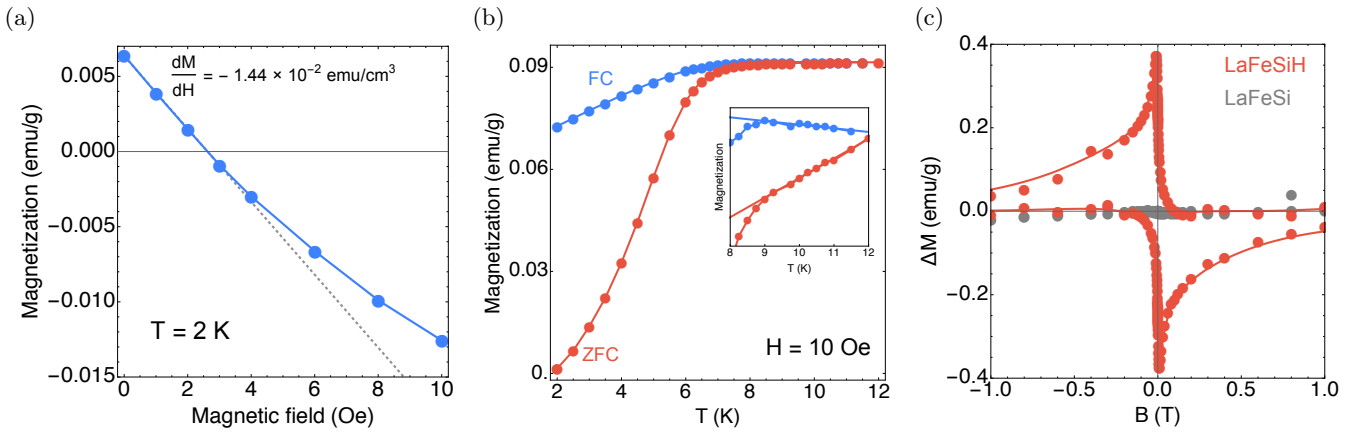


FIG. 5. (a) Magnetization as a function of the external field at 2 K (sam1). The strength of the global susceptibility  $dM/dH = -1.44 \times 10^{-2} \text{ emu/cm}^3$  is orders of magnitude higher than that of the best diamagnetic material (pyrolytic carbon) and hence confirms the emergence of superconductivity. (b) Magnetization as a function of temperature at  $H = 10 \text{ Oe}$  (sam2). The deviation from the linear behavior shown in the inset reveals the onset of superconductivity at  $T_c \gtrsim 9 \text{ K}$ . (c) Superconducting hysteresis loop obtained from the magnetization loop at 2 K (below  $T_c$ ) by subtracting by the loop at 10 K (above  $T_c$ ) (sam2). The gray points correspond to the same subtraction for the non-hydrogenated original LaFeSi powder, which contains the same secondary ferromagnetic phases but is not superconductor (and hence displays no hysteresis).

bon, *i.e.* the best non-superconducting diamagnetic material, and therefore demonstrates the presence of superconductivity without any doubt. In fact, this gives an lower-bound value for the superconducting diamagnetic strength since it includes a sizable ferromagnetic contribution from the additional non-superconducting phases (see below). For the same reason, the value  $H_{c1} \sim 3 \text{ Oe}$  that can be deduced for the lower critical field from the change in the slope has to be taken as a lower-bound value. In any case, the measured magnetization as a function of temperature confirms this superconducting behavior with a transition temperature  $T_c \simeq 9 \text{ K}$  as can be seen in Fig. 5(b) (see also Supplemental Material).

Furthermore, the observed change in the magnetization between 10 K and 2 K in the ZFC curve reveals a superconductor volume fraction of  $\sim 64 \%$  that has to be attributed to bulk superconductivity in LaFeSiH.

We notice that the overall magnetization of our samples is qualitatively dominated by the ferromagnetic signal of the additional phases (see Fig. S3 in Supplemental Material). However, this signal is essentially temperature independent below 10 K because it sets in at a much higher temperature [ $T_{\text{FM}} = 1044 \text{ K}$  for  $\alpha\text{-Fe}$  [16] and  $233\text{-}336 \text{ K}$  for  $\text{La}(\text{Fe},\text{Si})_{13}\text{H}_x$  [17]]. Thus, by subtracting the magnetic loop obtained at 10 K from the one at 2 K we can obtain the remaining contribution due to LaFeSiH. The resulting hysteresis loop is shown in Fig. 5(c). This loop unambiguously demonstrates that the hysteretic low-temperature behavior of this compound is superconducting in origin (see e.g. [18]).

The electric resistance of our powder samples reveals a Fermi-liquid behavior in the low temperature regime [see Fig. S4(a) in Supplemental Material] followed by a resistivity drop below  $\sim 10 \text{ K}$  [see Fig. 6(a)]. This drop is naturally explained by the emergence of superconductivity in LaFeSiH, even if the incomplete percolation of the current through the powder prevents the zero resistance [19]. In fact, its dependence on the applied magnetic field is characteristic of superconductivity. As customary, we determine the onset of superconductivity as a function of the applied field from the intersection of two extrapolated lines reproducing the resistance before and after the drop. The resulting values of the upper critical field  $H_{c2}$  are shown in the inset of Fig. 6(a). Using these values and the Werthamer-Helfand-Hohenberg formula  $H_{c2}(0) = -0.69 T_c dH_{c2}(T)/dT|_{T_c}$

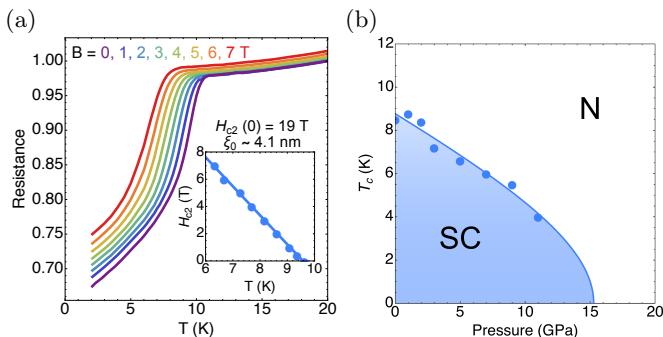


FIG. 6. (a) Low-temperature resistance as a function of temperature for different values of the applied magnetic field measured in sam2. Data are normalized to the value at 20 K and 0 T. The inset shows the upper critical field as a function of temperature obtained from these data. (b) Onset temperature of the superconducting transition  $T_c$  as a function of pressure obtained from resistance measurements in sam1.

we find  $H_{c2}(0) \simeq 19$  T and the zero-temperature correlation length  $\xi(0) \equiv \{\Phi_0/[2\pi H_{c2}(0)]\}^{1/2} \simeq 4.1$  nm. The value of these parameters indeed correspond to typical values for iron-based superconductors.

In addition, we determine the onset of superconductivity as a function of pressure from similar transport measurements [see Fig. S4(c)]. Thus, we find that the onset  $T_c$  decreases with pressure in a rather smooth fashion as can be seen in Fig. 6 (b). This behavior has a resemblance to the observed for the orthorhombic distortion [see Fig. 3], and hence suggests a strong interplay between the corresponding instabilities. The re-emergence observed in the orthorhombic distortion, however, is not observed for the superconductivity below 21 GPa.

*Conclusions.*— The synthesis of the novel hydride LaFeSiH inaugurates a supplementary track to understanding the rich physics of iron-based materials. This system displays structural, magnetic and electronic features characteristic of previously reported compounds. Namely, a low-temperature tetragonal to orthorhombic distortion likely related to antiferromagnetic order and a multiband quasi-2D Fermi surface largely dominated by Fe-3d orbitals. Most importantly, this compound demonstrates the possibility of iron-based superconductivity in a pnictogen- and chalcogen-free fashion. Thus, beyond its fundamental significance from both chemistry and physics point of view, LaFeSiH is expected to stimulate further research towards practical applications of iron-based superconducting materials.

We acknowledge ESRF for provision of beamtime at ID27 and M. Mezouar for fruitful discussions. F. B. acknowledges partial support from PRIN Grant No. 2012X3YFZ2\_004, the FP7 European project SUPER-IRON (grant agreement No. 283204), and Progetto biennale d’ateneo UniCA/FdS/RAS CUP F72F16003050002. A.C. acknowledges support from French Government “Investments for the Future” Program, University of Bordeaux Initiative of Excellence (IDEX Bordeaux), and Sardinia Regional Government “Visiting Professor” Program 2015, University of Cagliari.

---

\* andres.cano@cnrs.fr

- [1] A. Martinelli, F. Bernardini, and S. Massidda, *Comptes Rendus Physique* **17**, 5 (2016); E. Bascones, B. Valenzuela, and M. J. Calderón, *Comptes Rendus Physique* **17**, 36 (2016); D. S. Inosov, *Comptes Rendus Physique* **17**, 60 (2016); A. E. Böhmer and C. Meingast, *Comptes Rendus Physique* **17**, 90 (2016); Y. Gallais and I. Paul, *Comptes Rendus Physique* **17**, 113 (2016); A. van Roekeghem, P. Richard, H. Ding, and S. Biermann, *Comptes Rendus Physique* **17**, 140 (2016); F. Rullier-Albenque, *Comptes Rendus Physique* **17**, 164 (2016); S. Zapf, D. Neubauer, K. W. Post, A. Kadau, J. Merz, C. Clauss, A. Löhle, H. S. Jeevan, P. Gegenwart, D. N. Basov, and M. Dressel, *Comptes Rendus Physique* **17**, 188 (2016); P. J. Hirschfeld, *Comptes Rendus Physique* **17**, 197 (2016).
- [2] G. Garbarino, P. Toulemonde, M. Álvarez-Murga, A. Sow, M. Mezouar, and M. Núñez-Regueiro, *Phys. Rev. B* **78**, 100507 (2008); G. Garbarino, R. Weht, A. Sow, A. Sulpice, P. Toulemonde, M. Álvarez-Murga, P. Strobel, P. Bouvier, M. Mezouar, and M. Núñez-Regueiro, *Phys. Rev. B* **84**, 024510 (2011).
- [3] R. Welter, B. Malaman, and G. Venturini, *Solid State Communications* **108**, 933 (1998).
- [4] X. Liu, S. Matsuishi, S. Fujitsu, and H. Hosono, *Phys. Rev. B* **85**, 104403 (2012).
- [5] H. O. Jeschke, I. I. Mazin, and R. Valentí, *Phys. Rev. B* **87**, 241105 (2013).
- [6] Y. Zou, Z. Feng, P. W. Logg, J. Chen, G. Lampronti, and F. M. Grosche, *Physica Status Solidi Rapid Research Letters* **8**, 928 (2014).
- [7] J. Chen, K. Semeniuk, Z. Feng, P. Reiss, P. Brown, Y. Zou, P. W. Logg, G. I. Lampronti, and F. M. Grosche, *Phys. Rev. Lett.* **116**, 127001 (2016).
- [8] H. Kim, S. Ran, E. D. Mun, H. Hodovanets, M. A. Tanatar, R. Prozorov, S. L. Bud’ko, and P. C. Canfield, *Philosophical Magazine* **95**, 804 (2015).
- [9] S. Iimura, S. Matsuishi, H. Sato, T. Hanna, Y. Muraba, S. W. Kim, J. E. Kim, M. Takata, and H. Hosono, *Nat. Commun.* **3**, 943 (2012).
- [10] M. Hiraishi, S. Iimura, K. M. Kojima, J. Yamaura, H. Hiraka, K. Ikeda, P. Miao, Y. Ishikawa, S. Torii, M. Miyazaki, I. Yamauchi, A. Koda, K. Ishii, M. Yoshida, J. Mizuki, R. Kadono, R. Kumai, T. Kamiyama, T. Otomo, Y. Murakami, S. Matsuishi, and H. Hosono, *Nature Physics* **10**, 300 (2014).
- [11] R. Welter, I. Ijjaali, G. Venturini, and B. Malaman, *Journal of Alloys and Compounds* **265**, 196 (1998).
- [12] S. Tencé, G. André, E. Gaudin, P. Bonville, A. F. Al Alam, S. F. Matar, W. Hermes, R. Pottgen, and B. Chevalier, *Journal of Applied Physics* **106**, 033910 (2009); *Journal of Alloys and Compounds* **480**, 43 (2009); *Inorganic Chemistry* **49**, 4836 (2010).
- [13] T. Yildirim, *Phys. Rev. Lett.* **101**, 057010 (2008).
- [14] A. Cano, M. Civelli, I. Eremin, and I. Paul, *Phys. Rev. B* **82**, 020408 (2010).
- [15] A. Cano and I. Paul, *Phys. Rev. B* **85**, 155133 (2012).
- [16] J. M. D. Coey, *Magnetism and Magnetic materials* (Cambridge University press, New York, 2009).
- [17] A. Fujita, S. Fujieda, Y. Hasegawa, and K. Fukamichi, *Phys. Rev. B* **67**, 104416 (2003).
- [18] F.-C. Hsu, J.-Y. Luo, K.-W. Yeh, T.-K. Chen, T.-W. Huang, P. M. Wu, Y.-C. Lee, Y.-L. Huang, Y.-Y. Chu, D.-C. Yan, and M.-K. Wu, *Proceedings of the National Academy of Sciences* **105**, 14262 (2008).
- [19] The strong dependence on the morphology of the (cold-pressed non-sintered) powder demonstrates that the residual resistance of the sample is due to the incomplete percolation of the current [see Fig. S4(b)].